Supplementary Information (SI) for Lab on a Chip.

LFC-*plus*: Simultaneous Multicolor Volume Cytometry for High-Throughput Single-Cell Analysis

Zhi Ling[1,2,3,4], Wenhao Liu[1,2,3], Kyungduck Yoon[1,2,3,4], Zijun Gao[1,2,3,5], Keyi Han[1,2,3], Mithila Sawant[6,7], Aparna Kesarwala[6,7], and Shu Jia[1,2,3,†]

[1]*Laboratory for Systems Biophotonics, Georgia Institute of Technology, Atlanta, GA, USA*
[2] *Wallace H. Coulter Department of Biomedical Engineering, Georgia Institute of Technology and Emory University, Atlanta, GA, USA*
[3]*Parker H. Petit Institute for Bioengineering and Biosciences, Georgia Institute of Technology, Atlanta, GA, USA*
[4]*George W. Woodruff School of Mechanical Engineering, Georgia Institute of Technology, Atlanta, GA, USA*
[5]*School of Materials Science and Engineering, Georgia Institute of Technology, Atlanta, GA, USA*
[6]*Department of Radiation Oncology, Emory University School of Medicine, Atlanta, GA, USA*
[7]*Winship Cancer Institute, Emory University, Atlanta, GA, USA*
[†]*shu.jia@gatech.edu*

Supplementary Information contains:

1. LFC-*PLUS* SETUP

System design of the two-color Fourier light-field microscope. The Fourier light-field microscopy system [Fig. S1, Table S1] was equipped with a water-dipping objective lens (CFI75 LWD 16×/0.8NA W, Nikon) for a long working distance and a large imaging FOV [1]. Samples were epi-illuminated by two single-color cold visible mounted light-emitting diodes (LEDs), peaked at 470 nm (M470L5, Thorlabs) and 590 nm (M590L4, Thorlabs) simultaneously. Two achromatic doublets (AC254-200-A-ML and AC254-400-A-ML, Thorlabs) were inserted between the objective lens and the LED to form Kohler illumination. The fluorescence emitted from the sample was collected by the objective lens and was filtered by the dichroic mirror (ZT 405/488/594rpc-UF2, 50.8 mm × 72 mm × 2 mm, Chroma) and a corresponding emission filter (ZET 488/594m, 50 mm diam, Chroma), then divided by a 50:50 plate non-polarized beam splitter (#35-947, Edmund optics, diced into 72.5 mm × 50 mm × 1 mm) into two paths: a wide-field path focused by a tube lens (TTL200-A, Thorlabs; f_{FL} = 200 mm) and recorded by an sCMOS camera (Zyla 4.2, Andor; pixel size, 6.5 μm), and a light-field path focused by a 300-mm tube lens (AC508-300-A-ML, Thorlabs) on the native image plane (NIP), then Fourier transformed with a 200-mm Fourier lens (AC508-200-A-ML, Thorlabs) and focused by a customized microlens array (f_{MLA} = 30 mm, pitch size = 3.3 mm, diced from planoconvex lens of 20 mm diameter round by Edmund optics). The signals were filtered by corresponding customized micro filters (3.3 mm × 3.3 mm × 1 mm, ET520/40m for green channel, ET632/60m for the red, Chroma) to form an array of two-color images, which were captured on a second sCMOS camera (ORCA-Flash-4.0 v3, Hamamatsu) at a full-sensor frame rate of 100 Hz.

All 9 filters were embedded in the notch: 5 emission filters for the red channel, in the center and the four corners; and 4 filters for the green channel, in the four positions next to the center. The middle of the mount is a 3D-printed round plate with a 25 mm diameter and 4.4 mm thickness, with a 9.9 mm square hole in the center and 4 holes at the edges. Microlenses were placed as a 3×3 array in the center holes of the plate. The positions of the bottom plate's pillars coincide with the positions of the edge holes on the middle plate, and the hole and pillar diameters are nearly the same (the pillars are smaller), so the two plates can be connected using the holes and pillars. On top of the middle plate, a 25 mm-diameter round plate was placed. In the center of the top plate, there was a square notch of 12.55 mm side length and 1.5 mm depth, and a square aperture of 10 mm side length, where a window (Edmund #23-301) was embedded. Like the bottom plate, the top plate had four pillars that connected it to the middle plate.

Analytical throughput of the two-color LFC. The ***analytical cell throughput*** can be calculated by:

$$N = u \times S / \Delta v \tag{S1}$$

where u is the flow speed of the cell, S is the cross-sectional area of the microfluidic channel, and Δv is the volume occupied by each individual cell.

Stroboscopic illumination enables higher cell speeds while limiting motion blur (defined here as a maximum movement of 2 pixels per exposure), though it comes at the cost of reduced signal-to-noise ratio. In our setup, the maximum achievable flow speed u_m can be estimated as:

$$u_m = \frac{R_{xy}}{\Delta t} \tag{S2}$$

where $R_{xy} = 3.6$ μm is the lateral pixel resolution, and Δt can be as low as 100 μs. Our system has a cross-sectional area of 980 μm × 400 μm. Assuming a spacing between adjacent cells of twice the cell diameter (~20μm), the analytical throughput N is estimated to exceed 500,000 cells per second, underscoring the system's distinct advantage among existing IFC techniques (Fig. S13).

Here, the cell throughput is estimated based on the flow rate, where the cell arrival rate is determined by dividing the flow speed by the average cell-to-cell spacing. This calculation assumes that the detector is fast enough to resolve each passing cell within this interval. In the current setup, the sCMOS sensor operates at a maximum frame rate of 100 Hz. However, when integrated with advanced detectors such as single-photon avalanche diode (SPAD) sensors—capable of achieving frame rates from several thousand up to tens of thousands of frames per second—the throughput of the light-field system could approach its theoretical limit.

On the other hand, the ***theoretical imaging throughput*** can be estimated from the camera frame rate and the number of cells captured within a single frame, under the assumption that all cells present in the current frame move entirely out of the field of view by the next frame. This condition requires a minimum flow speed of

$$u_{min} = \frac{980\mu m}{100ms} = 9.8 \times 10^{-3} m/s$$

This speed is far above the threshold velocity (3.6×10^{-2} m/s), which would induce motion blur under stroboscopic illumination of 100 μs. With the camera operating at its full frame rate of 100 Hz, each frame can capture approximately 2,000 cells (Figure S8), resulting in a theoretical imaging throughput of up to 200,000 cells per second.

Resolution. The lateral resolution can be determined by the diffraction limit of the microlens, given as

$$R_{xy} = \frac{\lambda}{2NA_{MLA}} \times \frac{f_{\mathrm{FL}}}{f_{\mathrm{MLA}}} \times \frac{1}{M_{epi}}$$

$$NA_{MLA} = \frac{d_{MLA}}{2f_{MLA}}$$

Where d_{MLA} is the diameter of the aperture after the microlens, f_{FL}, and f_{MLA} are the focal lengths of the Fourier lens and the microlens, respectively, M_{epi} is the magnification at the native image plane.

The axial resolution can be calculated directly from ray optics. In our case, it is given as

$$R_z = \frac{\lambda {f_{\mathrm{FL}}}^2}{d_{MLA} \times d_1} \times \frac{1}{{M_{epi}}^2}$$

Where d_1 is the distance between the center of the furthest microlens to the central microlens.

The FOV is determined by the image area after each individual microlens. It depends on the size and focal length of the microlens and the focal length of the FL, given as

$$FOV = d_1 \times \frac{f_{\mathrm{FL}}}{f_{\mathrm{MLA}}} \times \frac{1}{M_{epi}}$$

The DOF can be obtained from the full-width half-maximum value of the PSF behind the central microlens on the optical axis along the axial direction. Theoretically, the axial FWHM value of the PSF of the central microlens

$$DOF = \frac{N^2\lambda}{NA^2} + \frac{N^2\lambda}{2S_r NA^2}$$

Where $S_r = \frac{\lambda}{2NA_{MLA}} \times \frac{M_{epi}}{P}$, P is the pixel size, $N = R_{xy}\frac{2NA}{\lambda}$

In short, increasing the numerical aperture (NA) of the system improves the spatial resolution but reduces the depth of field. The field of view (FOV) is closely related to the microlens pitch size at the current magnification—that is, the center-to-center distance between adjacent microlenses. A larger separation between microlenses enables the system to capture greater angular diversity, enhancing its ability to distinguish points along the axial (z) direction.

The Fourier light-field microscopy (FLFM) system **does not achieve diffraction-limited spatial resolution** compared with conventional wide-field microscopy, as the microlens array partitions the Fourier plane into sub-apertures to capture angular information from multiple perspectives within a single snapshot. The partitioning reduces the system's numerical aperture and thus its resolution. However, FLFM offers a distinct advantage by enabling **volumetric imaging without mechanical scanning**, achieving an **enhanced temporal resolution** up to two orders of magnitude faster, and **instrumentally simple operation** on epi-fluorescence platforms. Specifically, the current configuration (16X) is optimized for imaging organ- or tissue-scale samples with spatial range up to a millimeter and thicknesses of hundreds of micrometers, providing an extended depth range, at the cost of lateral and axial resolution. For instance, imaging a 400-μm-thick sample that would otherwise require approximately 250 axial scans with a 1.6-μm step size can be accomplished in a single exposure—an especially critical benefit when imaging dynamic or motion-prone samples. Therefore, the light-field flow cytometry system offers a unique opportunity for 3D imaging of microfluidics

systems, facilitating high-throughput 3D visualization and multiparametric analysis of multicellular dynamics and microenvironments.

2. DEBYE THEORY AND RECONSTRUCTION ALGORITHM

Derivation of wave function from a wave-optics model. FLFM is a linear system that projects and compresses a 3D objective volume onto a 2D camera chip. The 2D intensity image $I_c(\rho_c)$ taken by FLFM thus can be described as the convolution of the intensity distribution $I_o(r_o)$ of the isotropic emitters in the objective space and the (point spread function) PSF $\mathrm{PSF}(r_o, \rho_c)$ of the FLFM system, which is the square of the real part of the wave function $\mathrm{U}(r_o, \rho_c)$ of the FLFM system:

$$I_c(\rho_c) = \int \mathrm{PSF}(r_o, \rho_c)\, I_o(r_o)\, dr_o = \int |\mathrm{Re}[\mathrm{U}(r_o, \rho_c)]|^2\, I_o(r_o)\, dr_o \tag{S3}$$

where $r_o = (x_o, y_o, z_o) \in \mathbb{R}^3$ is the radius vector of the fluorescent emitters in objective space and $\rho_c = (x_c, y_c) \in \mathbb{R}^2$ gives the positions of pixels on the sensor plane. In practical calculation, both the objective volume and the sensor plane are discretized so that the relationship between the camera image I_c and the fluorescent intensity field I_o of the sample can be described as the product of matrix,$I_c = HI_o$, where H is the measurement matrix which is determined by the PSF and whose elements $h_{j,k} = \mathrm{PSF}\left(r_{o\,j}, \rho_{c_k}\right)$ denotes the contribution from the kth voxel in the objective domain to the intensity on the *j*th pixel on the camera sensor. Therefore, the reconstruction is mathematically an inverse process to recover I_o from a given I_c, and a maximum likelihood estimation can be gained by a modified deconvolution algorithm based on the Richardson-Lucy iteration scheme [3, 4]:

$$I_o^{(k+1)} = \mathrm{diag}\left\{\mathrm{diag}\left\{H^T H I_o^{(k)}\right\}^{-1} (H^T I_c)\right\} g^{(k)} \tag{S4}$$

where the operator diag{} diagonalizes a matrix. Therefore, the key point in retrieving the sample information from a raw light-field image via deconvolution is to acquire the PSF of the FLFM system. To gain the PSF, the wave function $U(r_o, \rho_{\mathrm{NAT}})$ of a point emitter is at first calculated on the native image plane (NIP) via Debye theory, considering a high numerical aperture (NA) objective is used [5]:

$$U(r_o, \rho_{\mathrm{NAT}}) = \frac{\mathrm{M_{obj}}}{f_{\mathrm{obj}}^2 \lambda^2} \exp\left[-\frac{iu}{4\sin^2(\alpha/2)}\right] \int_0^{\alpha} P(\theta) \exp\left[\frac{iu \sin^2\left(\frac{\theta}{2}\right)}{2\sin^2\left(\frac{\alpha}{2}\right)}\right] J_0\left[\frac{\sin(\theta)}{\sin(\alpha)} v\right] \sin(\theta)\, d\theta \tag{S5}$$

where $\rho_{\mathrm{NAT}} = (x_{\mathrm{n}}, y_{\mathrm{n}})$ represents the x and y coordinates on NIP, f_{obj} and M being respectively the focal length and magnification of the objective, and J_0 is the zeroth-order Bessel function of the first kind. The variable v denotes normalized radial coordinate, defined as $v = k[(x_{\mathrm{o}} - x_{\mathrm{n}})^2 + (y_{\mathrm{o}} - y_{\mathrm{n}})^2]^{1/2} \sin(\alpha)$, while u denotes normalized axial optical coordinates, defined as $u = 4kz_{\mathrm{o}} \sin^2(\alpha/2)$. The half-angle of the numerical aperture $\alpha = \sin^{-1}(\mathrm{NA}/n)$ and the wave number $k = 2\pi n/\lambda$ are calculated using the wavelength λ and the index of refraction n of the sample. For Abbe-sine corrected objectives, the apodization function of the microscope $P(\theta) = \cos(\theta)^{1/2}$ in this case. In our setup, f_{obj} is 12.5 mm, M is 16, and λ peaks at 525 nm and 630 nm. The refractive index n is 1.33 for the water solution.

Secondly, the propagation of the wavefunction $U(r_o, \rho_{\mathrm{NAT}})$ onto the camera plane can be simulated by successively transforming $U(r_o, \rho_{\mathrm{NAT}})$ into its Fourier space, as $\mathcal{F}[U(r_o, \rho_{\mathrm{NAT}})]$, timed $\mathcal{F}[U(r_o, \rho_{\mathrm{NAT}})]$ by a phase mask Φ, which represents the modulation of the MLA, and finally projecting the result $\mathcal{F}[U(r_o, \rho_{\mathrm{NAT}})]\, \Phi$ onto the sensor plane using optical Fourier transformation:

$$\mathrm{U}(r_o, \rho_c) = \mathcal{F}^{-1}\left\{\begin{array}{c} \mathcal{F}\left[\mathcal{F}[U(r_o, \rho_{\mathrm{NAT}})]\, \Phi(\rho_\mu)\right] \times \\ \exp\left[i2\pi f_{\mathrm{MLA}} \sqrt{\left(\frac{1}{\lambda}\right)^2 - \left(f_x^2 + f_y^2\right)}\right] \end{array}\right\} \tag{S6}$$

in which the exponential term is the transfer function of the Fresnel diffraction integral, and f_x and f_y are the x and y spatial frequencies in the sensor plane. $\Phi(\rho_\mu)$ is the phase modulation function at the point $\rho_\mu = (\rho_{\mu x}, \rho_{\mu y}) \in \mathbb{R}^2$ on the MLA. As the modulation of the entire lens array, it can be described by the convolution of a limited 2D comb

function $\mathrm{comb}(\rho_\mu/d_1)$ with the phase modulation function of a single lenslet, which is a combination of an input rectangular amplitude mask $\mathrm{rect}(\rho_\mu/d_1)$, a phase mask $\exp\left(\frac{-ik}{2f_{\mathrm{MLA}}}\|\rho_\mu\|_2^2\right)$, and an output spherical amplitude mask $\mathrm{circ}(\rho_\mu/d_{\mathrm{MLA}})$:

$$\Phi(\rho_\mu) = \mathrm{comb}\left(\frac{\rho_\mu}{d_1}\right) \otimes \left[\mathrm{rect}\left(\frac{\rho_\mu}{d_1}\right) \exp\left(\frac{-ik}{2f_{\mathrm{MLA}}}\|\rho_\mu\|_2^2\right) \mathrm{circ}\left(\frac{\rho_\mu}{d_{\mathrm{MLA}}}\right)\right] \tag{S7}$$

where f_{MLA}= 30 mm, d_{MLA}= 1.3 mm are respectively the focal length, the diameter (aperture) of a single lens, while d_1= 3.3 mm is the pitch of the MLA. $\otimes$ denotes the convolution operator.

Different from the single-color FLFM [1], the experimental PSF of the two-color FLFM was collected using fluorescent microspheres with two excitation/emission peaks, illuminated simultaneously with two light sources. This setup generated two-color elemental images corresponding to the two emission filters. Similarly, hybrid PSFs were obtained by aligning the experimental PSF peaks at each z-plane with the simulated profiles.

Reconstruction based on the Richardson-Lucy deconvolution scheme. The 3D deconvolution iteratively conducts a forward projection ($HI_o^{(k)}$), which projects the 3D object space onto the 2D camera plane and a backward projection ($H^T I_c$and $H^T HI_o^{(k)}$) which takes the inverse process. As the FLFM system is spatially-invariant, PSF at a depth of z can be described as the intensity contribution from an emitter located on the optical axis, i.e., $r_o = (0, 0, z_o)$. As a result, the forward projection can be simplified as a sum of 2D convolution on different layers within an axial range $[z_-, z_+]$, i.e.,

$$HI_o^{(k)} = \sum_{z_o=z_-}^{z_o=z_+} \mathrm{PSF}(\rho_c, z_o) \otimes I_o^{(k)}(z_o) \tag{S8}$$

where $I_o^{(k)}(z_o)$ represents the intensity distribution given by the single-layer objects at a depth of z_o. Similarly, the simplified back-projection form is given as:

$$H^T I_c(z_o) = \sum_{z_o=z_-}^{z_o=z_+} \mathrm{PSF}'(\rho_c, z_o) \otimes I_c(z_o) \tag{S9}$$

$$H^T HI_o^{(k)}(z_o) = \sum_{z_o=z_-}^{z_o=z_+} \mathrm{PSF}'(\rho_c, z_o) \otimes HI_o^{(k)}(z_o) \tag{S10}$$

where $\mathrm{PSF}'(\rho_c, z_o)$ is obtained by rotating $\mathrm{PSF}(\rho_c, z_o)$ by 180 degrees.

Hybrid point spread function. For conventional light field microscopy, either an experimentally measured or numerically simulated PSF is used for volumetric reconstruction. The experimental PSF faithfully records the deviation of PSF caused by optical aberrations due to misalignment of the system and its difference from a theoretical PSF due to the fabrication error of the MLA. However, the information about the details of the PSF is usually lost in the inevitable image noise, especially in greater depths, rendering artifacts in the reconstructed volume. On the other hand, the simulated PSF, in single or double precision, is free of noise and maintains the continuity of intensity values, which challenges the experimental PSF recorded by a sCMOS camera. However, it contains no information about the mismatch between the MLA used in practice and the theoretically simulated phase mask, causing artifacts or deviated information in the reconstruction. Therefore, a hybrid PSF method was developed which combined the information of both the experimental and numerical PSF with enhanced image quality [1, 4]. First, the position of the brightest pixel in the experimental PSF was linearly fitted and interpolated in the axial direction to the full range of the simulated PSF. At each axial position, the intensity profile of the numerical PSF was shifted to the location of the corresponding experimental results. Through the calibration process, deviations of reconstruction were minimized while achieving a consistent high SNR to avoid computational artifacts across the entire imaging depth. A standard volumetric reconstruction using Richardson–Lucy deconvolution requires approximately 20 seconds for 10 iterations when executed on an RTX 3090 GPU.

3. DATA PROCESSING AND ANALYSIS

Model-based correction of sCMOS-related noise. A fluorescence microscopy noise correction method designed for sCMOS cameras [6] was applied to the raw elemental images to enhance the signal-to-noise ratio compromised by the short exposure time of stroboscopic illumination. First, the noisy input image was rescaled using pixel maps of offset and gain. Next, the noise variation was estimated from the intensity distribution of a high-pass filtered image

with the threshold set at the optical transfer function (OTF) boundary, determined by the effective *NA* of the system, which can be calculated based on our previously reported results:

$$NA_{eff} = \frac{d_{\mathrm{MLA}}}{2f_{\mathrm{FL}}}\frac{f_{\mathrm{TL}}}{f_{\mathrm{obj}}} \quad (S11)$$

Here d_{MLA} is the aperture size of a single microlens, f_{obj}, f_{TL}, f_{FL} and are the focal lengths of the objective lens, the tube lens, and the Fourier lens, respectively [7].

This estimated variation was then used as a parameter for sparse denoising, where each reference patch was grouped with similar patches into a 3D array, and collaborative Wiener filtering was performed using a 3D transform [8]. Due to the similarity among patches, the 3D transform provides a sparser representation of the original patches than the 2D transforms. Finally, the aggregation procedure returns the denoised patches to their original locations. Multi-core CPU computing is used to accelerate the computation.

Cell segmentation and volumetric calculation. For high-throughput statistical analysis of cells in the 3D IFC images, cell segmentation was performed using a customized method (Fig. S12). First, the initial center of each cell was identified by locating the local maxima in the smoothed 3D reconstructed volume. A binarized volume was then generated using Otsu's thresholding method. Within each non-connected binary cluster, the detected cell centers were used to further separate the cluster into individual cells through k-means clustering with center initialization. This approach offers more efficient segmentation compared to other algorithms, such as watershed methods, which are typically better suited for higher-resolution images. For dual-labeled cells (nuclei and membranes), the nuclei channel was used to determine the cell center, and the same separation strategy was applied. Only cells with both nuclei and membranes identified were included in the statistical analysis. Finally, the volume, intensity, surface area, and sphericity of each segmented cell were quantified. The volume is the number of voxels within each segmented mask. The intensity is the sum of all the intensity values within each segmented mask. The sphericity is defined as:

$$\varphi = \frac{\pi^{\frac{1}{3}}(6 \times volume)^{\frac{2}{3}}}{surface\ area} \quad (S12)$$

Analysis of stiffness-dependent 3D secondary flow-driven cell migration in curved channels. Equilibrium positions of cells/particles in the flow arise from a balance between the shear gradient lift force and the wall-induced lift force, both acting perpendicular to the main flow direction. The shear gradient lift force results from the velocity gradient in the fluid flow, typically highest in the center and decreasing towards the walls, pushing particles towards the region of lower velocity near the wall. Wall-induced lift force arises from the asymmetry of the fluid flow around a particle when it's near a wall. The wall disrupts the flow, creating a pressure difference that pushes the particle away from the wall.

In the straight section of a microchannel, the velocity profile follows fully developed Poiseuille flow, exhibiting asymmetry with the maximum velocity point located along the centerline of the channel due to the balance of the shear gradient and wall-induced lift forces. In contrast, in curved channel geometry, the Poiseuille flow is subjected to the centrifugal force, which disturbs the parabolic profile. The velocity peak shifts from the center towards the concave wall of the channel. The sharp gradient near the wall induces secondary flow recirculation, generating two counter-rotating vortices, commonly referred to as Dean vortices, driven by the Dean drag force [9, 10].

After 3D reconstructions, cells from both fluorescence channels were segmented as described above. The nuclei channel was used for tracking all cells with the TrackMate plugin in ImageJ to analyze the speed distributions across the cross-sectional planes. For each trajectory, the distance to the channel centerline and the lateral position were calculated and plotted against cell speed. The velocity peak was closer to the concave side, as shown in Fig. 5 and Fig. S10. Next, dead cells were separated from live cells by recognizing the coexistence of Live-or-Dye signals and the SYTO 16 signals. In Fig. 5 (L, M), the centroid of each nucleus was computed in all 1000 frames (10 s), and the accumulated positions were used to generate trajectory density maps at each cross-section. A Gaussian blur was applied to aid in the visualization of cell distribution.

The velocity map showing the vortex directions typically requires COMSOL simulations. However, our 3D reconstruction captures the real-time positions of cells across different cross-sectional planes. Each xz cross-section shows two lateral high-density regions near the top and bottom of the channel, forming a pattern consistent with Dean vortices. Based on our results, dead (stiffer) cells tend to accumulate on one side of the channel, while normal live cells showed a broader distribution.

A dimensionless number called the Dean number (*De*) is used to quantify the magnitude of the two Dean vortices and is given by:

$$De = Re\sqrt{\frac{D_h}{2R}} = \frac{\rho U_f D_h}{\mu}\sqrt{\frac{D_h}{2R}} \quad (S13)$$

where μ is the fluid viscosity, U_f is the mean fluid velocity, R is the curve radius of the convex surface of the curved channel, D_h is the hydraulic diameter of the channel, and Re is the dimensionless channel Reynolds number. With a flow rate of 15 μL/min and R = 100 μm, it gives a Re number of 1.25 and a Dean number of 1.77. Due to the relatively slow flow rate in our cellular IFC imaging compared with conventional microfluidics experiments, the resulting Dean number is lower, indicating weaker Dean forces. Thus, 1000 frames of cross-sectional trajectories were accumulated for analysis.

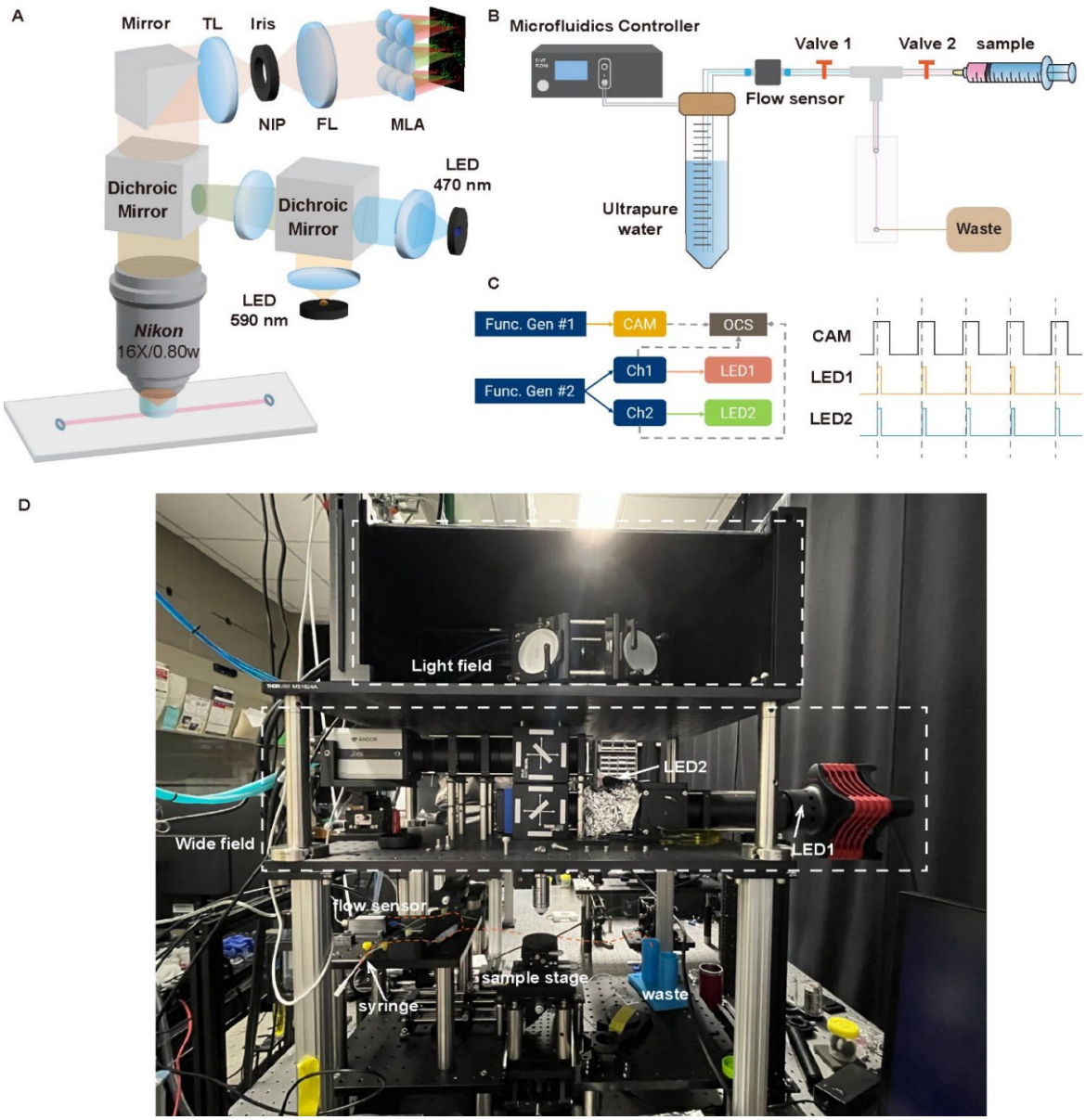

Figure S1.

Schematic (A, B, C) and photograph (D) of the experimental setup.

(A) LEDs peaked at 470 nm and 594 nm illuminate the sample simultaneously, forming an overlapped dual-color image at the native image plane (NIP). The image is then Fourier transformed by the Fourier lens (FL) and partitioned by a micro lens array, followed by an emission filter array to form an array of elemental images of two channels on the camera plane. OL, objective lens; TL, tube lens; DM, dichroic mirror; FL, Fourier lens; MLA, microlens array. (B) The microfluidic setup consists of a single-channel microfluidic flow controller, a microfluidic flow sensor, microfluidic chips, microfluidic reservoirs, a syringe, valves, and a waste tank. (C) Function generators trigger both the camera and the LEDs, enabling synchronization and stroboscopic illumination.

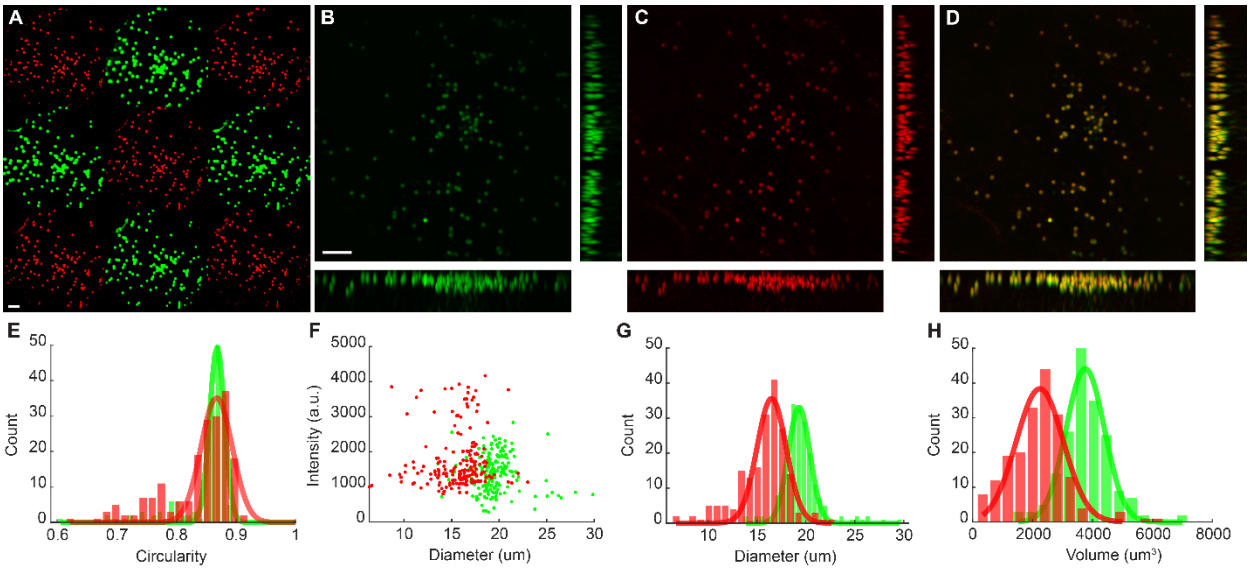

Figure S2.

Characterization of the LFC-*plus* using 16 µm fluorescent microspheres.

(A) Two-color Fourier light-field image of 16 µm diameter microspheres with two excitation/emission peaks, captured at the first time frame. (B-D) Max intensity projections of the reconstructed volume from (A), for the green (B) and red (C) channels, and as a merged image (D). (E) Histograms of the circularity values of 189 microspheres in both channels, peaked at 0.86 in the green channel and 0.88 in the red channel. (F) Relationship between the average single-cell intensity and diameter measured from reconstruction in both channels. (G, H) Histograms showing the distribution of the cell diameters 19.32 µm (green) and 16.22 µm (red) (G); and volumes, with median values of 3777 μm^3 (green) and 2235 μm^3 (red) (H). Scale bars: 100 µm (A-D).

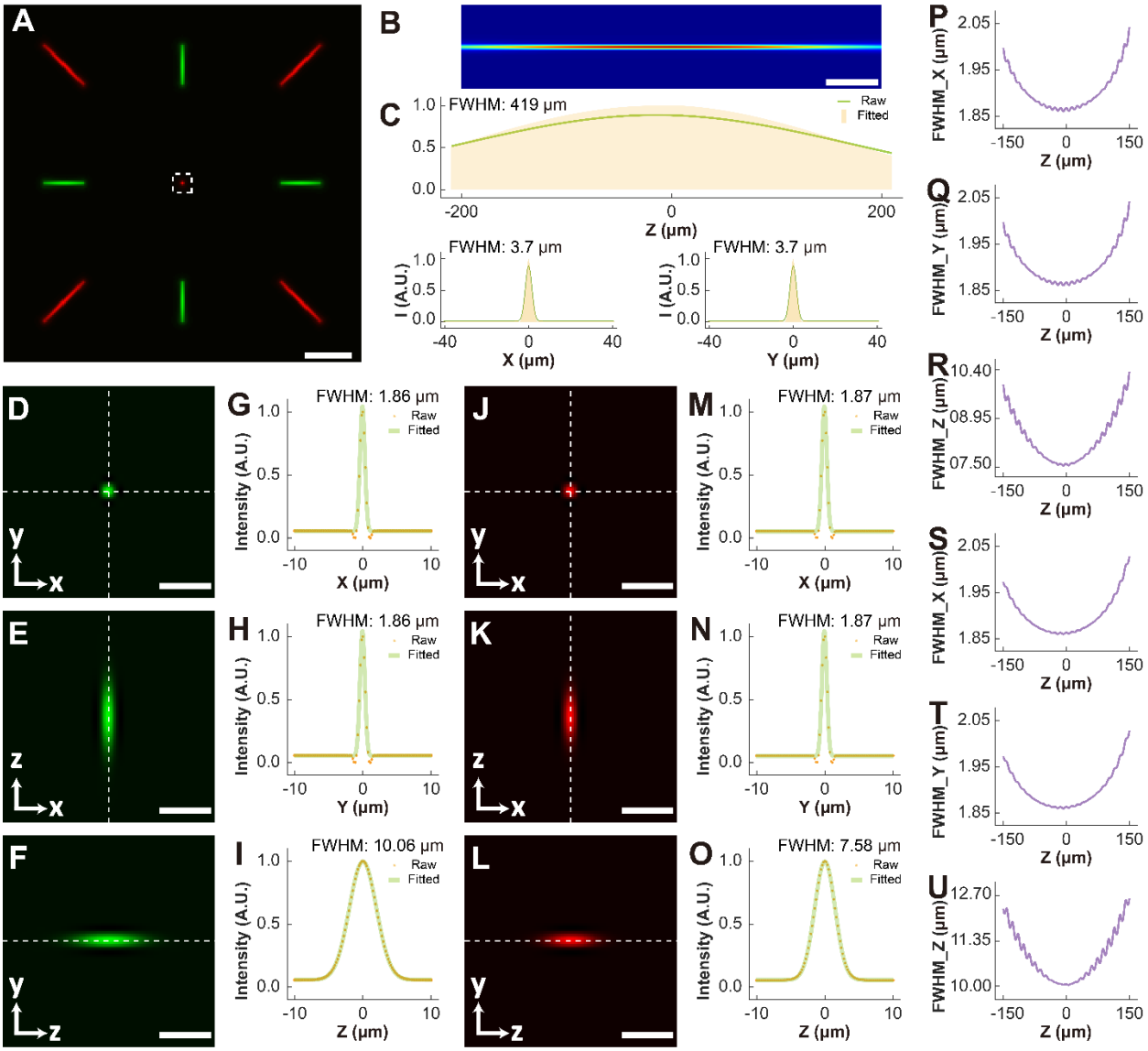

Figure S3.

System characterization using simulated PSF.

(A) 3D MIP of the stacks of simulated two-color PSF of a 400 μm axial range. (B) Cross-sectional image of the volume of the center sub-PSF as boxed in (A). (C) Plots of the 3D intensity profiles of the fitted 3D Gaussian function of the center sub-PSF along Z (upper panel), X (bottom left panel), and Y (bottom right panel). The z-profile exhibited a FWHM value of 419 μm, which corresponds to the depth of the field over 419 μm. The x and y profiles present FLFM values of 3.7 μm, corresponding to a lateral resolution of 3.7 μm, consistent with the system design. (D-F) Central cross-sections on xy (D), xz (E), and zy (F) planes, of the volume reconstructed from the simulated PSF on the focal plane in green channel through deconvolution using the simulated PSF via iteration of 20 times. (G-I) Plots of the 3D intensity profiles along the dashed lines in (D-F), along x (G), y (H), and z (I), respectively. They present an elliptical spot with FWHMs of 1.86 μm in x, 1.86 μm in y, and 10.06 μm in z. (J-L), Central cross-sections on xy (J), xz (K), and zy (L) planes, of the volume reconstructed from the simulated PSF on the focal plane in the red channel through deconvolution using the simulated PSF via iteration 20 times. (M-O) Plots of the 3D intensity profiles along the dashed lines in (J-L), along x (M), y (N), and z (O). They present an elliptical spot with FWHMs of 1.87 μm in x, 1.87 μm in y, and 7.58 μm in z. (P-R) The plots of FWHMs of the 3D profiles of reconstructed spots from simulated PSFs in the green channel on different layers, exhibiting the variation of spatial resolution of the red channel in x (P), y (Q), and z (R), with respect to the imaging depth. (S-U) The plots of FWHMs of the 3D profiles of reconstructed spots from simulated PSFs in the red channel on different layers, exhibiting the variation of spatial resolution of the red channel in x (S), y (T), and z (U), with respect to the imaging depth. Scale bar: 50 μm (A, B), 10 μm (D-F, J-L).

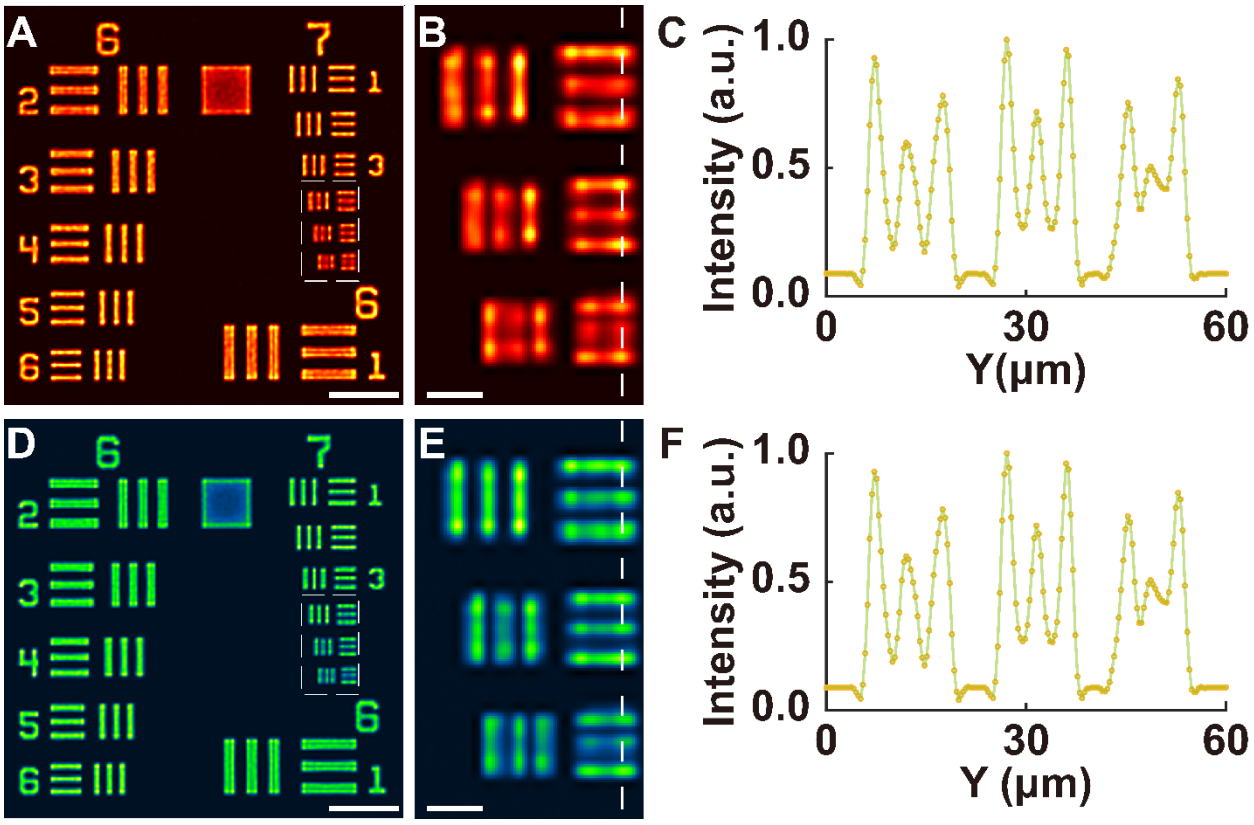

Figure S4.

Resolution measurement using the fluorescent USAF 1951 target.

(A) Fluorescent USAF 1951 target reconstruction from the red channel of the IDC-FLFM image. (B) Zoomed-in image of the dashed region in (A). (C) Profile of the dashed line in (B). (D) Fluorescent USAF 1951 target reconstruction from the green channel of the IDC-FLFM image. (E) Zoomed-in image of the dashed region in (D). (F) Profile of the dashed line in (E). The images demonstrated that element 6 in group 7 of the USAF element can be reconstructed in both green and red channels, corresponding to a lateral resolution of 2.19 μm. Scale bars: 50 μm (A, D), 10 μm (B, E).

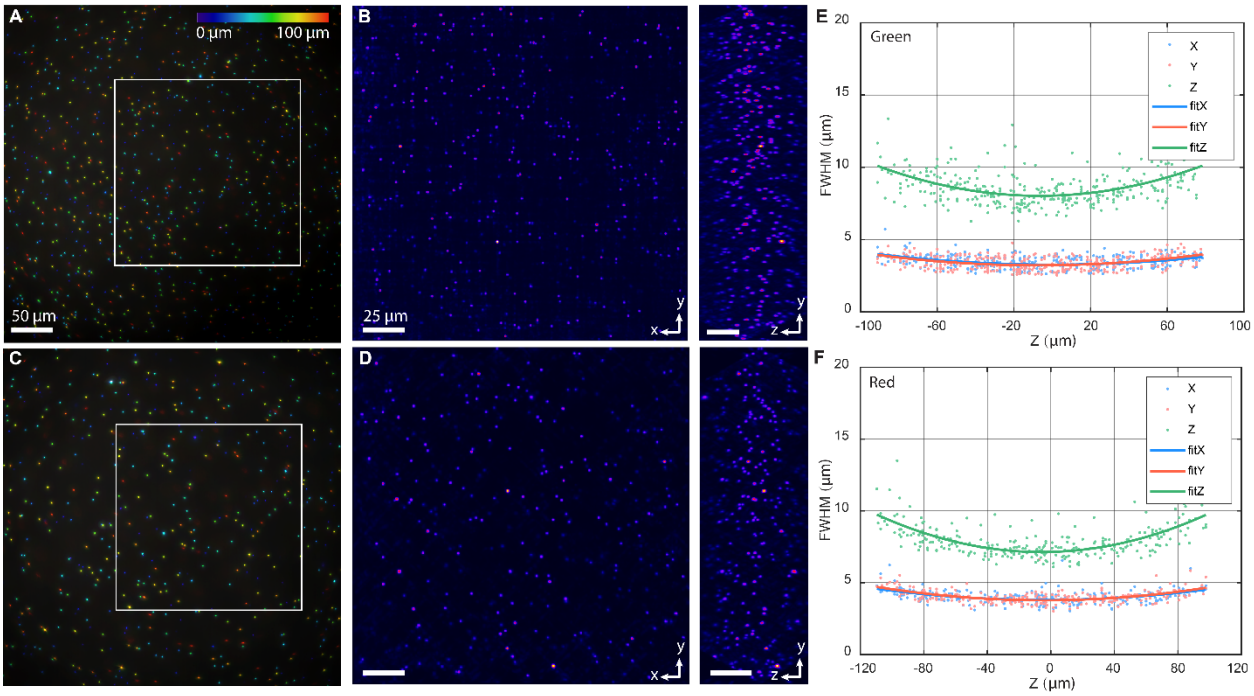

Figure S5.

System characterization using 2 µm fluorescent microspheres.

(A, C) Depth-color-coded wide-field z-stacks across a 100 µm axial range with a step size of 0.4 µm, showing green (A) and red (C) beads of 2 µm embedded in a 3D agarose gel. (B, D) 3D reconstructions at the corresponding field of view in the boxed region in (A) and (C), demonstrating recovery of a larger axial depth. (E, F) Full width half maximum (FWHM) values of the 3D cross-sectional profiles at varying depths over a 200 µm axial range, exhibiting 3.2 - 4.0 µm and 8.0 - 10.1 µm for the green channel (E); 3.7 - 4.7 µm and 7.1 - 9.7 µm in the lateral and axial dimensions for the red channel (F), respectively.

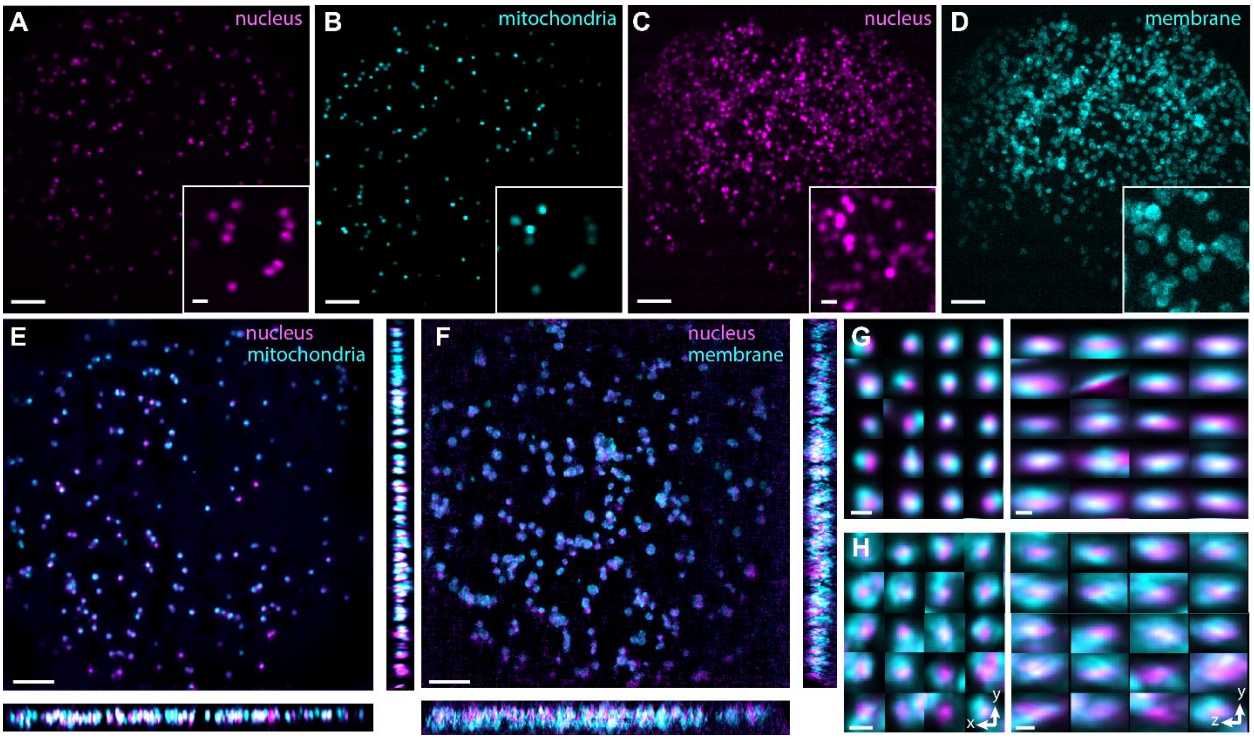

Figure S6.

Imaging different subcellular structures in flowing HeLa cells using the LFC-*plus*.

(A, B) Elemental two-color light-field images of the nuclei (A) and mitochondria (B) of HeLa cells, labeled with SYTO 16 and MitoTracker Red, captured at the first time frame. (C, D) Elemental two-color light-field images of the nuclei (C) and membranes (D) of HeLa cells labeled with SYTO 16 and WGA 594 in the first time frame. Insets show the distinct subcellular structures from corresponding regions. (E, F) MIP of the 3D reconstructed volumes from (A, B) in (E), and (C, D) in (F). (G, H) MIP images of a large population of cells in *xy* and *yz*, illustrating the spatial relationships between the mitochondria (G) and membranes (H) with the nuclei. Scale bars: 100 μm (A-F), 10 μm (G-H).

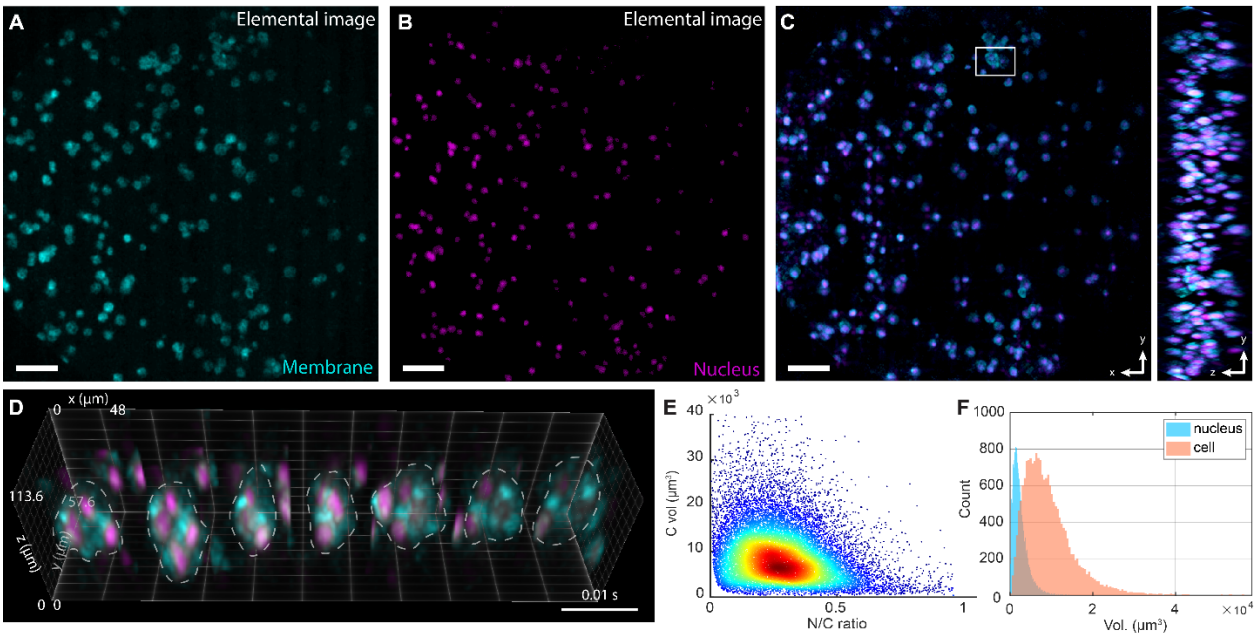

Figure S7.

Imaging mixed HeLa and H460 cells using the LFC-*plus*.

(A, B) Elemental two-color light-field images of cell membranes (A) and nuclei (B) of mixed HeLa and H460 cells labeled with SYTO 16 and WGA 594 captured at the first time frame. (C) MIP of the 3D reconstructed volume from (A, B). (D) 3D reconstructed volumes of the cells in the boxed region in (C) across 7 time frames, demonstrating the IFC system's ability to track cell motion in a large volumetric space. (E) Scatter density plot showing the relationship between cell volume (C vol) and the nuclear-to-cell (N/C) volume ratio for individual cells. (F) Histogram showing the volume distribution of nuclei (blue) and whole cells (orange) across 19499 cells counted within 100 frames, with median volumes of 1,946 μm³ for nuclei and 7,832 μm³ for whole cells. Scale bars: 100 μm (A-F).

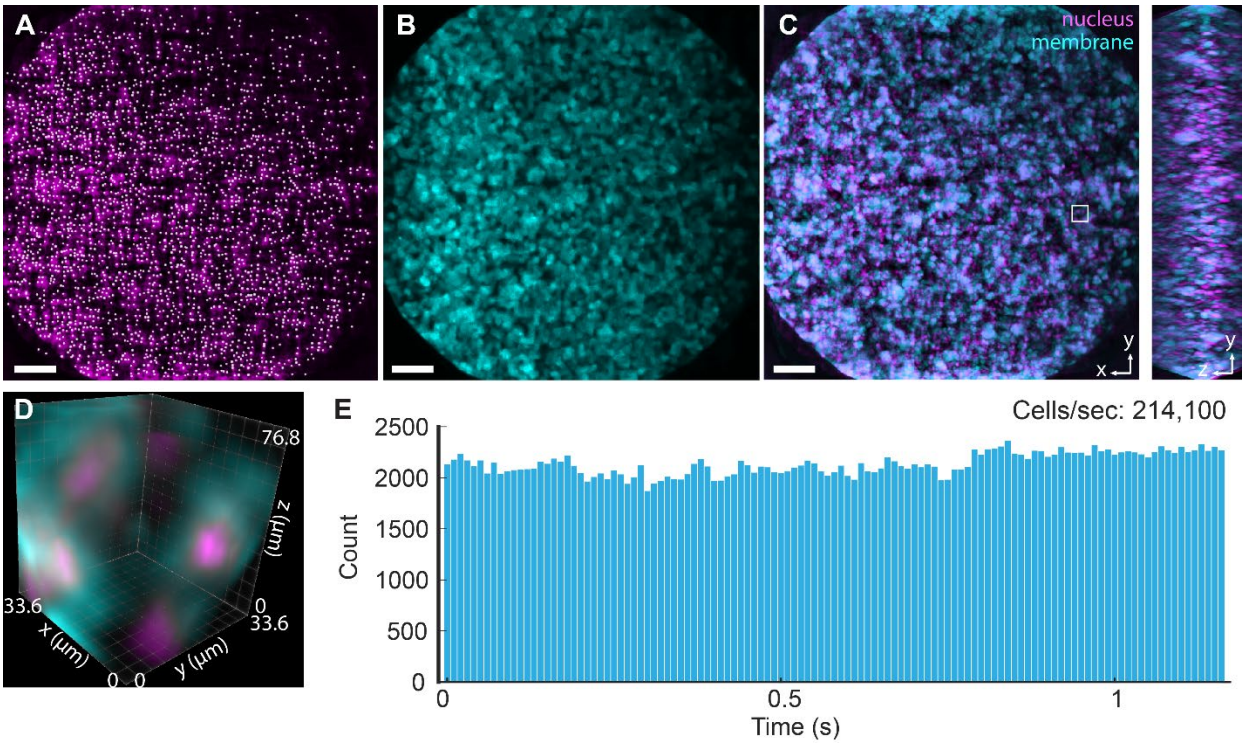

Figure S8.

Demonstration of imaging throughout using the LFC-*plus*.

(A, B) Elemental two-color light-field images of cell nuclei (A) and membranes (B) of HeLa cells labeled with SYTO 16 and WGA 594 captured at the first time frame. Each nucleus in (A) is marked with a white dot at its center. (C) MIP of the 3D reconstructed volume from (A, B). (D) 3D reconstructed volume of the cells in the boxed region in (C), showing the 3D spatial relationship between cell membrane and nuclei, highlighting the capacity of the IFC system to resolve densely packed cell populations in 3D. (E) Cell count over a 1.17-second interval, yielding an estimated throughput of 214,100 cells per second. Scale bars: 100 μm (A-C).

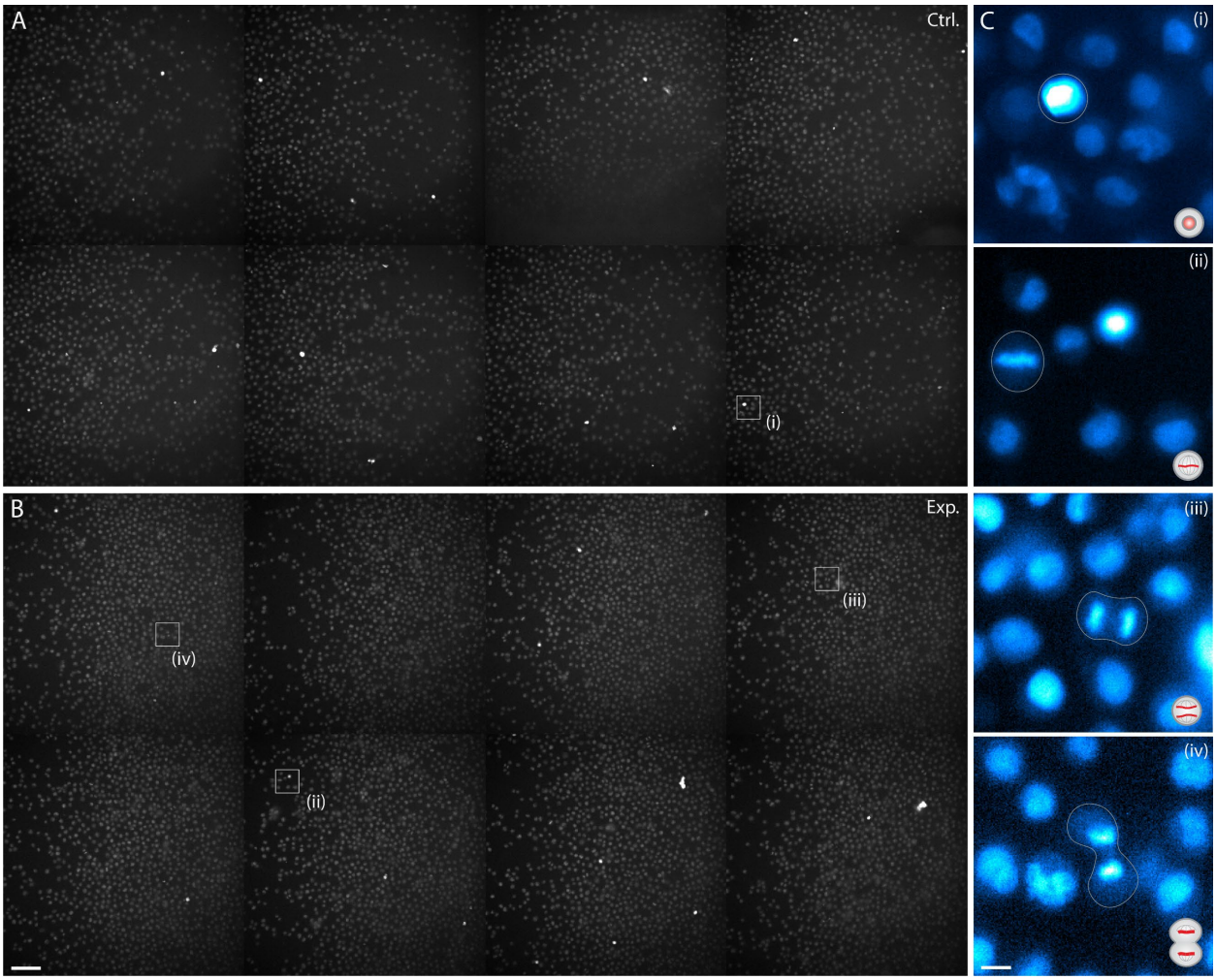

Figure S9.

Wide-field imaging of H460 in a microfluidic channel.

(A, B) Wide-field fluorescence images of the Lung Adenocarcinoma Cell (H460) labeled with PI from the control group (A) and the etoposide-treated group. (C) Zoom-in views of the white boxed regions marked from (i) to (iv) in (A) and (B), showing cells in different stages of mitosis. (i) The nuclear membrane breaks down to release the chromosomes. (ii) The chromosomes line up and attach to spindle microtubules. (iii) The chromosomes break at the centromere, and the microtubules pull the sister chromatids to opposite sides of the cell. (iv) Two new complete nuclei form, and the cell can divide into two daughter cells. A higher number of mitotic cells was observed in the experimental group, indicating drug-induced mitotic arrest during DNA replication. Scale bars: 100 μm (A, B), 10 μm (C).

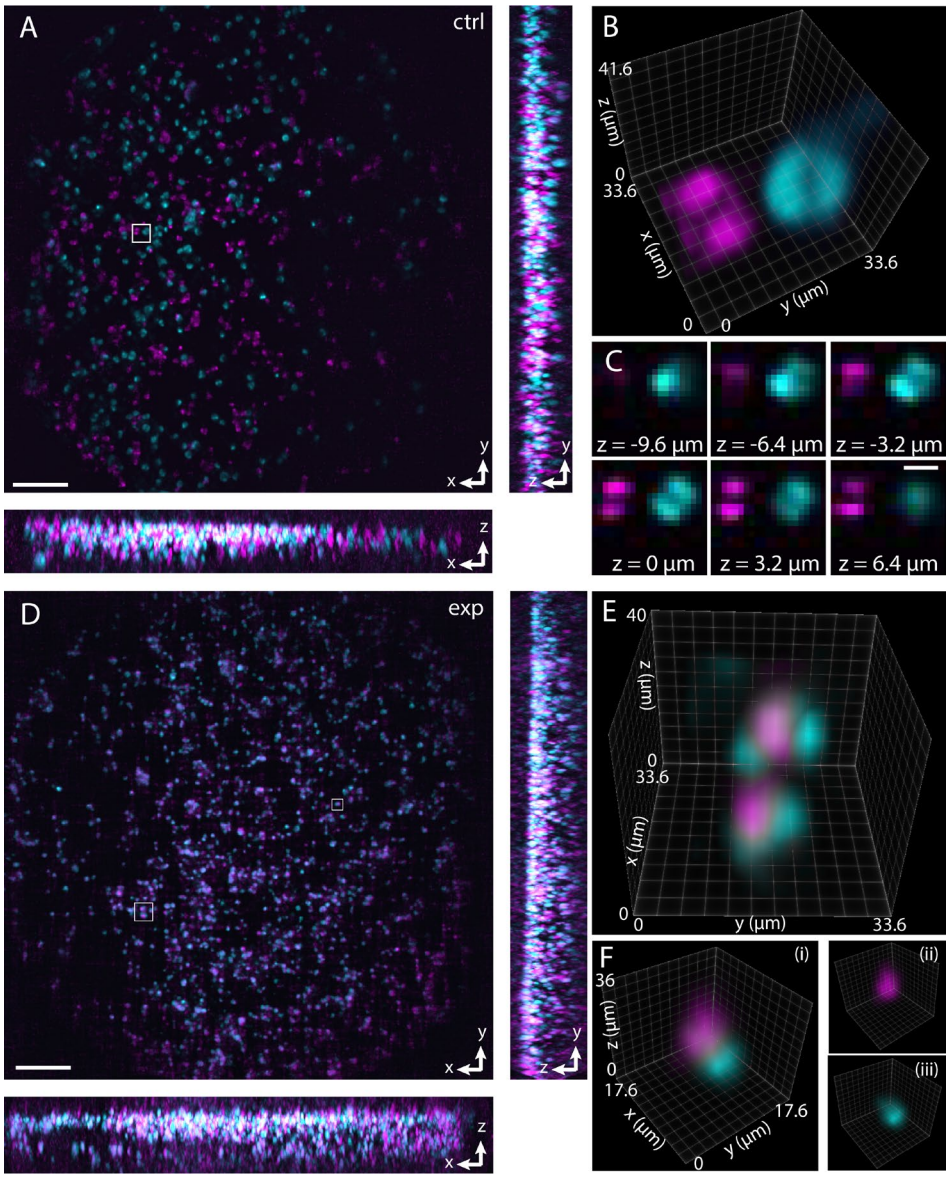

Figure S10.

Imaging PEG-mediated fusion of Jurkat cells using the LFC-*plus*.

(A) Maximum intensity projection (MIP) images of the 3D reconstructed volume of the control group at a single time frame. (B) 3D rendering of the boxed region in (A). (C) Axial slices of two separate Jurkat cells in (B) at different z depths, showing the morphology and the mitochondria distribution. (D) Maximum intensity projection (MIP) images of the 3D reconstructed volume of the experimental group at a single time frame. (E, F) 3D rendering of the boxed regions in (D), illustrating close contact between two groups of cells. Scale bars: 100 μm (A, D), 10 μm (C).

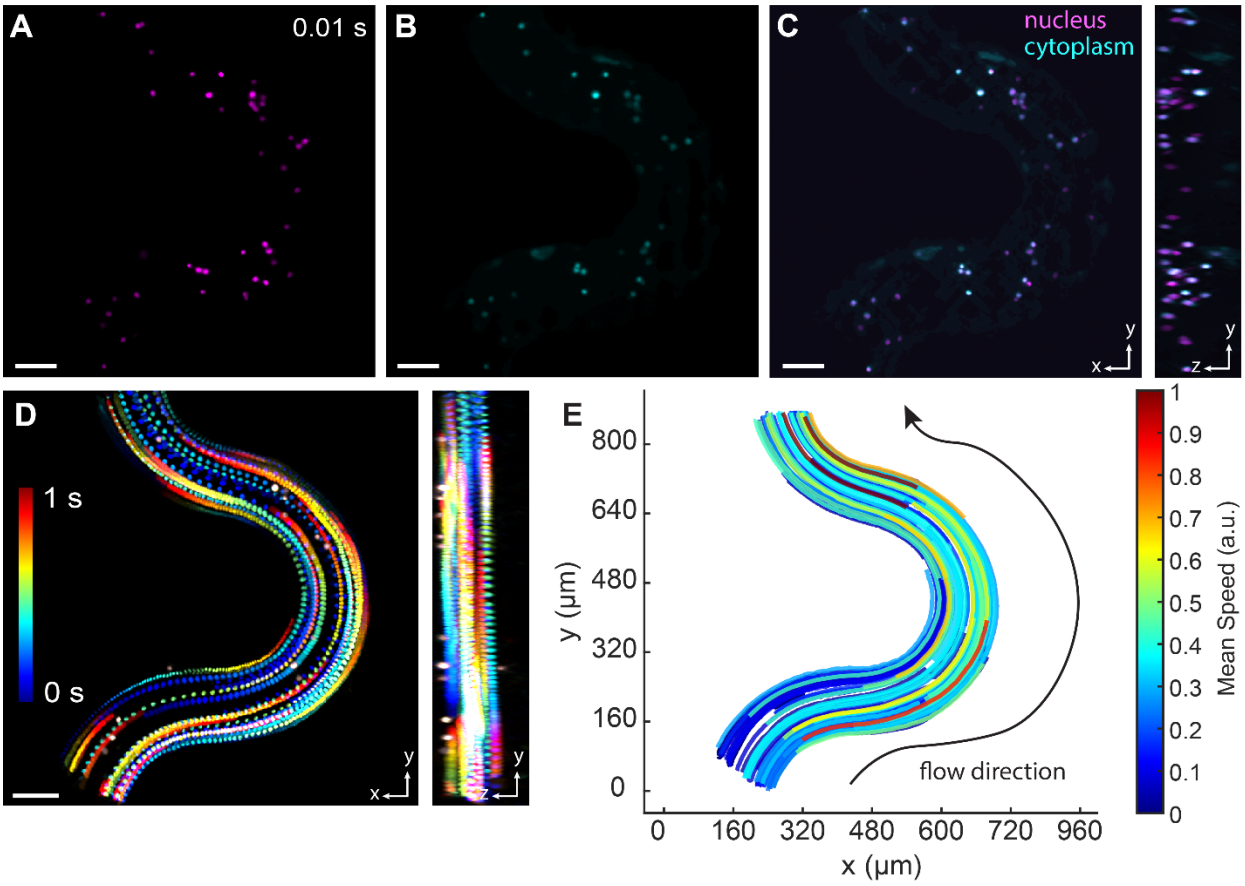

Figure S11.

Imaging live and dead HeLa cells in curved microfluidic channels using two-color IFC.

(A-C) Elemental two-color light-field images of nuclei (A) and cytoplasm (B) of HeLa cells labeled with SYTO16 and Live-or-Dye 594 captured at the first time frame. (C) MIP of the 3D reconstructed volume from (A) and (B), showing nuclei of all cells (magenta) and cytoplasm of dead cells (cyan). (D) Time-color-coded MIP of the reconstructed nuclei over 1 second at 10 ms intervals, visualizing cell trajectories through the curved channel. (E) Normalized cell speed map in the channel. The color of each trajectory indicates the cell's average speed over 1 second, with peak flow near the channel center and higher flow velocity near the outer wall than near the inner wall. Scale bars: 100 μm (A-D).

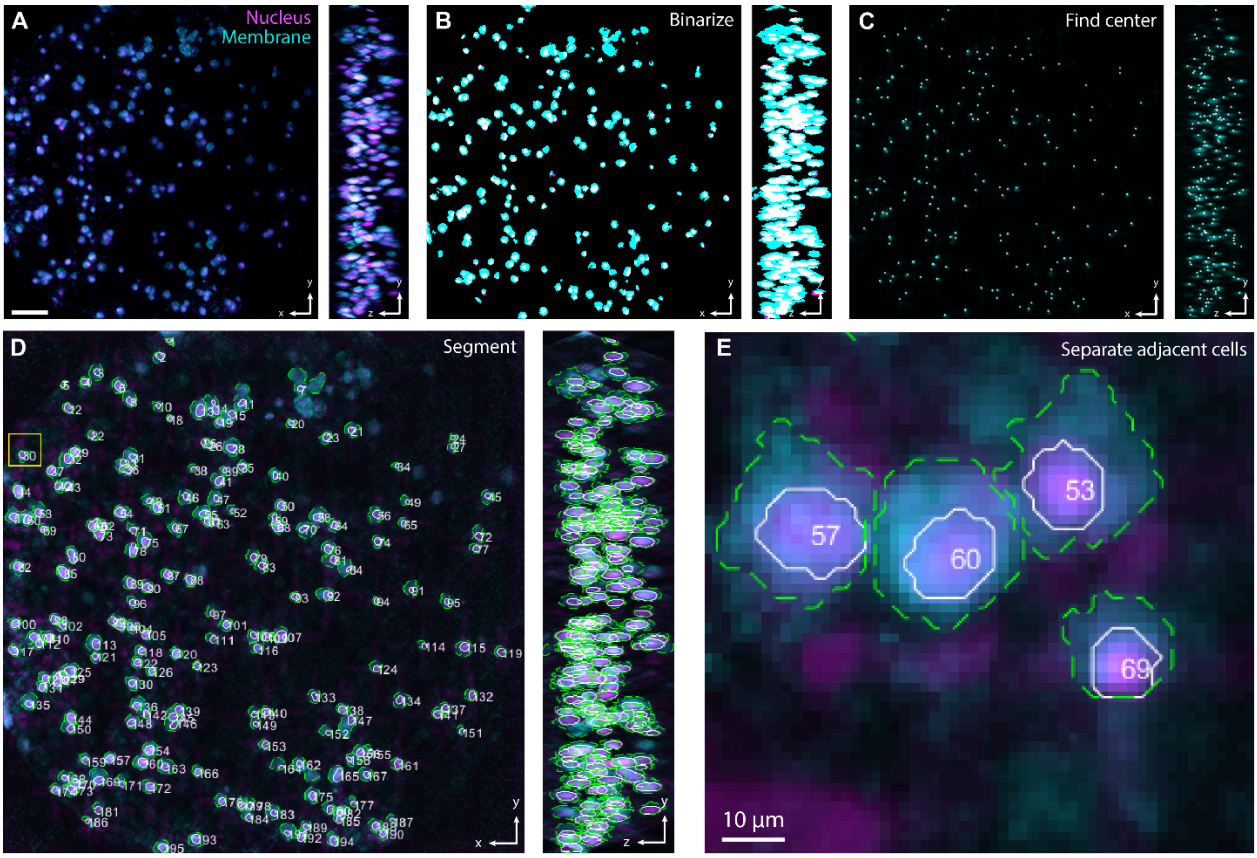

Figure S12.

3D segmentation of the two-color volumes reconstructed using two-color IFC.

(A) MIP of the 3D reconstructed volume of HeLa cells labeled with SYTO16 for nuclei (magenta) and WGA 594 for membranes (cyan). (B) Binarized 3D volumes using Otsu's thresholding method. (C) Centers of individual cells, identified by locating the 3D intensity maximum of the nuclei channel, marked with white dots. (D) Segmented 3D MIP masks for each cell, showing nuclei and membrane boundaries outlined in white and green, respectively. Segmentation was achieved by separating each connected cluster based on the local maxima. (E) Zoomed-in image of the yellow boxed region in (D), highlighting the effective separation of closely packed cells. Scale bars: 100 µm (A-D), 10 µm (E).

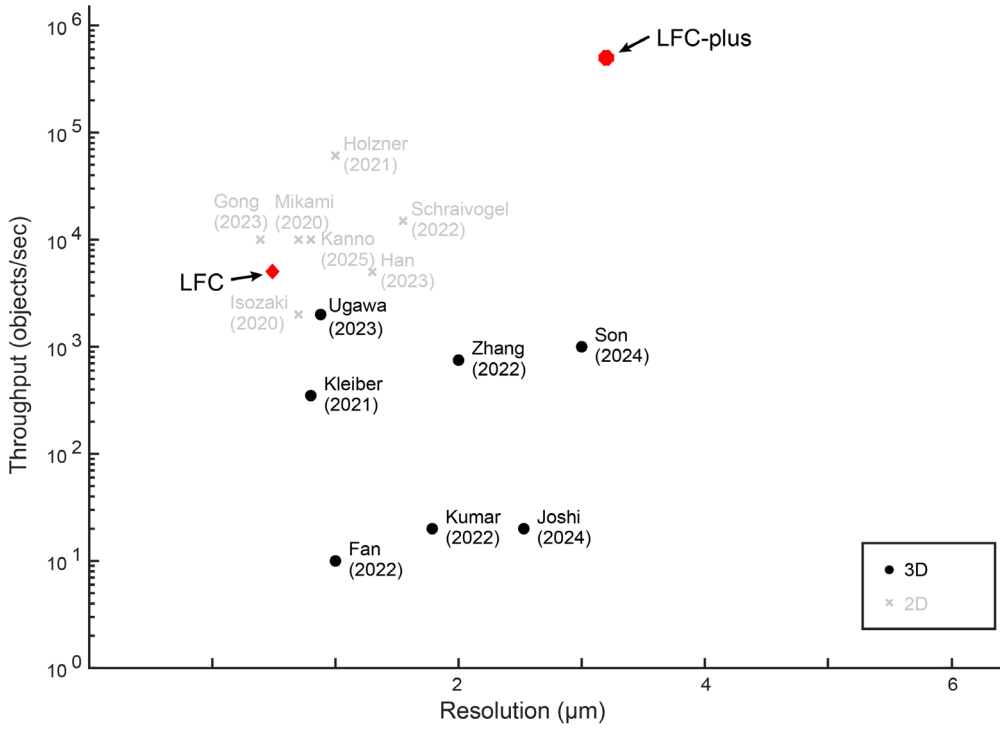

Figure S13.

Resolution vs. throughput chart for 2D and 3D IFC techniques in the past five years.

SUPPLEMENTARY TABLES

Fourier light-field microscope							
Objective lens	Tube lens	Fourier lens	MLA			Excitation Wavelength ± Bandwidth (nm)	
CFI75 LWD 16XW 16×, 0.8 NA WD 3 mm	f_{TL}: 300 mm	f_{FL}: 200 mm	f_{MLA}: 30 mm	P_{MLA}: 3.3 mm	d_{MLA}: 1.3 mm	480±20	594±5
Temporal Resolution	Spatial (xy) Resolution	Spatial (z) Resolution	FOV		DOF	Emission Wavelength ± Bandwidth (nm)	
100 Hz	3~4 μm	7~9 μm	Φ: 980 μm		400 μm	520±20	630±30

Table S1.
System performance of the two-color FLFM microscopy system.

References	Year	3D	Objective (M, NA)	Resolution (nm)	Throughput (objects/sec)	Imaging Instrument
This work **LFC-*plus***		yes	16×, 0.8	3,200	500,000 (theoretical cell throughput)	Fourier light-field microscope with micro filter arrays
Kanno, et al. (FLIM)[11]	2024	no	20×, 0.75	800	10,000	Dual intensity-modulated continuous-wave beam arrays
Hua, Han, et al. (LFC)[12]	2024	yes	100×, 1.45	400-600	5,000 (theoretical cell throughput)	Epi-fluorescence with MLA
Joshi, et al. (M3IC)[13]	2024	yes	10×, 0.3	2,530	20-30	Vertically aligned multi-sheet array (VAMSA) illumination
Son, et al. [14]	2023	yes	--,0.63	2000-4000	1,000	Portable light-sheet optofluidic microscopy
Han, et al. (LASE)[15]	2023	no	20×, 0.75	1,300	5,000	Linear array spot excitation
Gong, et al.[16]	2023	no	20×, 0.4	390	10,000	Anti-diffraction light sheet illumination
Ugawa, et al.[17]	2022	yes	20×, 0.75	880	2,000	Strobe light-sheet imaging
Kumar, et al. (VFC/iLIFE)[18]	2022	yes	20×, 0.4	1,786	10-20	Light-sheet microscopy
Zhang, et al.[19]	2022	yes	10×, 0.28	2,000	500-1,000	Scanning light-sheet illumination
Schraivogel, et al. (ICS)[20]	2022	no	10×, 0.3	1,550	15,000	Radiofrequency-tagged emission (FIRE)
Fan, et al.[21]	2021	yes	40×, 0.8	1,000	<10	Lattice light-sheet microscopy
Holzner, et al.[22]	2021	no	40×, 0.75 / 20×, 0.5 / 15× / 10×	500-1,000	5,350 (40×), 10,900 (20×), 20,500 (15×), 61,000 (10×)	Light-sheet illumination
Kleiber, et al.[23]	2020	yes	20×, 0.42	700-900	350	3D focusing tomography
Mikami, et al. (VIFFI)[24]	2020	no	20×, 0.75	700	10,000	Polygon scanner light-sheet illumination
Isozaki, et al. (iACS2.0)[25]	2020	no	20×, 0.75	700	2,000	Polygon scanner

Table S2.

Comparisons with the fluorescent IFC techniques in the past 5 years.

Feature	LFC (Hua, X., Han, K., et al., Nat. Commun. 2024)	LFC-*plus* (this work)
Fluorescence Channels	Single-color	Dual-color (simultaneous)
Volumetric Resolution	Submicron 3D resolution (~500 nm in *xy*, ~632 nm in *z*)	Subcellular 3D resolution (3.0 μm in *xy*, 8.0 μm in *z*)
Cell Throughput	Low-to-moderate (~5,000 cells/s)	High (~5×10^5 cells/s)
Field of View	Narrow region (~70 μm)	Extended spatial range (~mm scale)
Depth of Focus	Single cell layer (~6 μm)	Extended depth (~400 μm)
Optical Design	Microlens array-based LFM	Microlens array + spectral aperture partitioning
Temporal Acquisition Mode	Sequential single-frame acquisition	Simultaneous multicolor capture
Data Redundancy Handling	Requires sparse flow conditions	Reduced via spatial optimization
Microfluidic Compatibility	Narrow microfluidic channels	Flexible and structured channels
Usage	High-resolution single-cell imaging	High-throughput multiparametric analysis

Table S3.
Key differences between conventional LFC (Hua, X., Han, K., et al., *Nat Commun*, 2024)[12] and LFC-*plus* (this work).

Figure	Target	Label	Stroboscopic exposure time (μs)	Flow rate (μL/min)
2	HeLa, Jurkat	SYTO 16, WGA594	500	80
3	H460	PI	1,000	5~10
4	Jurkat-mixing	MitoTracker Green, MitoTracker Red	2,000	15
	Jurkat-fusion	MitoTracker Green, MitoTracker Red	1,000	5~10
5	HeLa	SYTO16, live-or-dye 594	800	10
S2	16 μm beads	--	200	<5
S3	2 μm beads	--	--	0
S4	HeLa	SYTO16, MitoTracker Red	2,000	5~10
		SYTO 16, WGA594	100	70
S5	HeLa, H460	SYTO 16, WGA594	500	70
S6	HeLa	SYTO 16, WGA594	300	150
S11	HeLa	SYTO16, live-or-dye 594	800	<5

Table S4.
Experimental configurations and fluorescent labels for the LFC.

LEGENDS FOR SUPPLEMENTARY VISUALIZATIONS

Visualization 1

3D MIP of time-lapse volumes of reconstructed HeLa and Jurkat cells in the flow imaged using LFC-*plus*, both labeled with SYTO 16 (magenta) and WGA 594 (cyan), as shown in **Fig. 2**. The images were taken at 100 Hz, and the reconstructed videos were over 9.01 s and played at 100 fps.

Visualizations 2, 3

3D MIP of time-lapse volumes of Lung Adenocarcinoma Cell (H460) labeled with PI in the control group (**Visualization 2**) and chemotherapy-treated group (**Visualization 3**) in the flow imaged using LFC-*plus*, as shown in **Fig. 3**. The images were taken at 100 Hz, and the reconstructed videos were over 10 s and played at 100 fps.

Visualizations 4, 5

3D MIP of time-lapse volumes of Jurkat cells labeled with MitoTracker Green or MitoTracker Red in the control group (**Visualization 4**) and PEG-mediated fusion group (**Visualization 5**) in the flow imaged using LFC-*plus*, as shown in **Fig. 4**. The images were taken at 100 Hz, and the reconstructed videos were over 10 s and 5 s and played at 100 fps.

Visualization 6

3D MIP of time-lapse volumes of live and heat-treated dead HeLa cells labeled with SYTO16 and Live-or-Dye 594 in a curved microfluidic channel in the flow imaged using LFC-*plus*, as shown in **Fig. 5**. The images were taken at 100 Hz, and the reconstructed videos were over 10 s and played at 100 fps.

REFERENCES

1. W. Liu, G.-A. R. Kim, S. Takayama and S. Jia, *Biosensors and Bioelectronics*, 2022, **208**, 114201.
2. A. Nascimento, J. Lannigan and D. Kashatus, *Cytometry A*, 2016, **89**, 708-719.
3. C. Guo, W. Liu, X. Hua, H. Li and S. Jia, *Opt Express*, 2019, **27**, 25573-25594.
4. X. Hua, W. Liu and S. Jia, *Optica*, 2021, **8**, 614-620.
5. *Advanced Optical Imaging Theory*, 2000.
6. B. Mandracchia, X. Hua, C. Guo, J. Son, T. Urner and S. Jia, *Nat Commun*, 2020, **11**, 94.
7. Z. Ling, W. Liu, K. Yoon, J. Hou, P. Forghani, X. Hua, H. Yoon, M. Bagheri, L. P. Dasi, B. Mandracchia, C. Xu, S. Nie and S. Jia, *Nat Cardiovasc Res*, 2025, DOI: 10.1038/s44161-025-00649-7.
8. K. Dabov, A. Foi, V. Katkovnik and K. Egiazarian, *IEEE Trans Image Process*, 2007, **16**, 2080-2095.
9. Y. Saffar, S. Kashanj, D. S. Nobes and R. Sabbagh, *Micromachines (Basel)*, 2023, **14**.
10. N. Nivedita, P. Ligrani and I. Papautsky, *Sci Rep*, 2017, **7**, 44072.
11. H. Kanno, K. Hiramatsu, H. Mikami, A. Nakayashiki, S. Yamashita, A. Nagai, K. Okabe, F. Li, F. Yin, K. Tominaga, O. F. Bicer, R. Noma, B. Kiani, O. Efa, M. Buscher, T. Wazawa, M. Sonoshita, H. Shintaku, T. Nagai, S. Braun, J. P. Houston, S. Rashad, K. Niizuma and K. Goda, *Nat Commun*, 2024, **15**, 7376.
12. X. Hua, K. Han, B. Mandracchia, A. Radmand, W. Liu, H. Kim, Z. Yuan, S. M. Ehrlich, K. Li, C. Zheng, J. Son, A. D. Silva Trenkle, G. A. Kwong, C. Zhu, J. E. Dahlman and S. Jia, *Nat Commun*, 2024, **15**, 1975.
13. P. Joshi, P. Kumar, A. S, J. M. Varghese and P. P. Mondal, *Communications Physics*, 2024, **7**.
14. J. Son, B. Mandracchia, A. D. Silva Trenkle, G. A. Kwong and S. Jia, *Lab Chip*, 2023, **23**, 624-630.
15. Y. Han, J. Zhao, Z. Chao, K. Liang, C. Zhang, L. Jiang, Z. Jiao, F. Bai, A. Tárnok and Z. You, *Device*, 2023, **1**.
16. Y. Gong, M. Zeng, Y. Zhu, S. Li, W. Zhao, C. Zhang, T. Zhao, K. Wang, J. Yang and J. Bai, *Micromachines (Basel)*, 2023, **14**.
17. M. Ugawa and S. Ota, *Biomed Opt Express*, 2022, **13**, 3647-3656.
18. P. Kumar, P. Joshi, J. Basumatary and P. P. Mondal, *Sci Rep*, 2022, **12**, 78.
19. Z. Zhang, R. Tang, X. Chen, L. Waller, A. Kau, A. A. Fung, B. Gutierrez, C. An, S. H. Cho, L. Shi and Y. H. Lo, *Proc Natl Acad Sci U S A*, 2022, **119**.
20. D. Schraivogel, T. M. Kuhn, B. Rauscher, M. Rodriguez-Martinez, M. Paulsen, K. Owsley, A. Middlebrook, C. Tischer, B. Ramasz, D. Ordonez-Rueda, M. Dees, S. Cuylen-Haering, E. Diebold and L. M. Steinmetz, *Science*, 2022, **375**, 315-320.
21. Y. J. Fan, H. Y. Hsieh, S. F. Tsai, C. H. Wu, C. M. Lee, Y. T. Liu, C. H. Lu, S. W. Chang and B. C. Chen, *Lab Chip*, 2021, **21**, 344-354.
22. G. Holzner, B. Mateescu, D. van Leeuwen, G. Cereghetti, R. Dechant, S. Stavrakis and A. deMello, *Cell Rep*, 2021, **34**, 108824.
23. A. Kleiber, A. Ramoji, G. Mayer, U. Neugebauer, J. Popp and T. Henkel, *Lab Chip*, 2020, **20**, 1676-1686.
24. H. Mikami, M. Kawaguchi, C. J. Huang, H. Matsumura, T. Sugimura, K. Huang, C. Lei, S. Ueno, T. Miura, T. Ito, K. Nagasawa, T. Maeno, H. Watarai, M. Yamagishi, S.

Uemura, S. Ohnuki, Y. Ohya, H. Kurokawa, S. Matsusaka, C. W. Sun, Y. Ozeki and K. Goda, *Nat Commun*, 2020, **11**, 1162.
25. A. Isozaki, H. Mikami, H. Tezuka, H. Matsumura, K. Huang, M. Akamine, K. Hiramatsu, T. Iino, T. Ito, H. Karakawa, Y. Kasai, Y. Li, Y. Nakagawa, S. Ohnuki, T. Ota, Y. Qian, S. Sakuma, T. Sekiya, Y. Shirasaki, N. Suzuki, E. Tayyabi, T. Wakamiya, M. Xu, M. Yamagishi, H. Yan, Q. Yu, S. Yan, D. Yuan, W. Zhang, Y. Zhao, F. Arai, R. E. Campbell, C. Danelon, D. Di Carlo, K. Hiraki, Y. Hoshino, Y. Hosokawa, M. Inaba, A. Nakagawa, Y. Ohya, M. Oikawa, S. Uemura, Y. Ozeki, T. Sugimura, N. Nitta and K. Goda, *Lab Chip*, 2020, **20**, 2263-2273.